Chapter 3

Crystal Structure and Microstructure

In this chapter,the analysis regarding the structure, microstructure, molecular structure and optical studies is presented. Crystal structure parameters like, space group, lattice constants, and Wyckoff positions of each element were determined using refinement methods. Microstructures were studied using Scanning Electron Microscopy.

3. X-Ray Diffraction (XRD) Studies

The quality of the prepared samples was studied using the XRD pattern taken with the help of monochromatic X-rays. Also, strain measurement and crystallite size were determined for all the samples.

Following methods have been used to calculate the crystalline size and strain:

Debye Scherrer method:

Crystallite size can be calculated by the line broadening method using the Scherrer equation given below [1]:

$$D = \frac{K\lambda}{\beta_D Cos\theta} \qquad (3.1)$$

D = particle size, λ = wavelength of the incident x-rays, K = Scherrer constant equal to 0.9, β_D is the peak width at half maxima, θ = peak position

Williamson-Hall plot:

The induced strain due to crystal imperfections and distortion causes line broadening and are related by thefollowing equation:

$$\varepsilon = \frac{\beta_s}{tan\theta} \qquad (3.2)$$

Where ε = average strain produced and β_s = strain-induced line broadening. The Debye-Scherrer method has **a** dependency on *1/cosθ*, but in Williamson-Hall analysis it depends on *tanθ*. This fundamental difference allows separation of such different causes of reflection broadening occurring together, i.e. due to small crystallite size and microstrain. Here it is assumed that the size and strain broadening arethe summative components of the total integral breadth of a Bragg Peak [2]. The foundation of the Williamson-Hall analysis is laid by such distinct dependencies of the above effects. On combining the equations (3.1) and (3.2), the strain-induced line broadening can be given by the equation [3]:

$$\beta = \beta_D + \beta_s \qquad (3.3)$$

Therefore

$$\beta cos\theta = \left(\frac{K\lambda}{D}\right) + (4\varepsilon sin\theta) \qquad (3.4)$$

The strain was considered uniform in the above equation in all crystallographic directions due to the isotropic nature of the crystal [2]. $\beta cos\theta$ was plotted against $4\mathcal{E}sin\theta$ where the slope and y-intercept of the fitted line represent strain and particle size, respectively.

Size-Strain plot method:

Size and strain measurements can also be done in a better manner using the "size-strain plot" (SSP) estimation. It has theadvantage of giving less weightage to the data from higher angleshaving less accuracy. In SSP, the strain profile by the Gaussian function and thecrystallite size profile is given by theLorentzian function[3]. The equation is given by:

$$(d\beta cos\theta)^2 = \frac{k\lambda}{D}(d^2\beta cos\theta) + \left(\frac{\varepsilon}{2}\right)^2 \qquad (3.5)$$

Where d = inter planer spacing and $K, \lambda, \mathcal{E}, \theta, \beta$ and D have their usual meanings as above. $(d\beta cos\theta)^2$ is plotted against $(d^2\beta cos\theta)$, from this particle size is calculated from the slope of the linearly fitted data, and the square root of the intercept gives the strain [3].

Also, Rietveld refinement of the XRD data of the samples of both the series provided us with useful information such as the refined unit cell parameters, Wyckoff positions of the elements, space group information, etc. The results are discussed and presented for two groups of series.

3.1 X-ray diffraction (XRD) analysis of pure and doped $CuFeO_2$

The samples in this series showed the effect of doping at the Fe site in the $CuFeO_2$ compound. Figure 3.1 shows the **X-ray** diffraction patterns for the pure $CuFeO_2$ and doped $CuFe_{0.96}M_{0.03}V_{0.01}O_2$ samples. Vanadium has been added 1% to stabilize the phase at 1273 K [4,5]. This type of effect has been reported earlier and it also improves grain formation. Beyond 2% doping of Eu had shown impurity phases in these samples [6]. The impurity phases have also been observed for the Ni doping above 2% [7] and Mn doping at 5% [8].

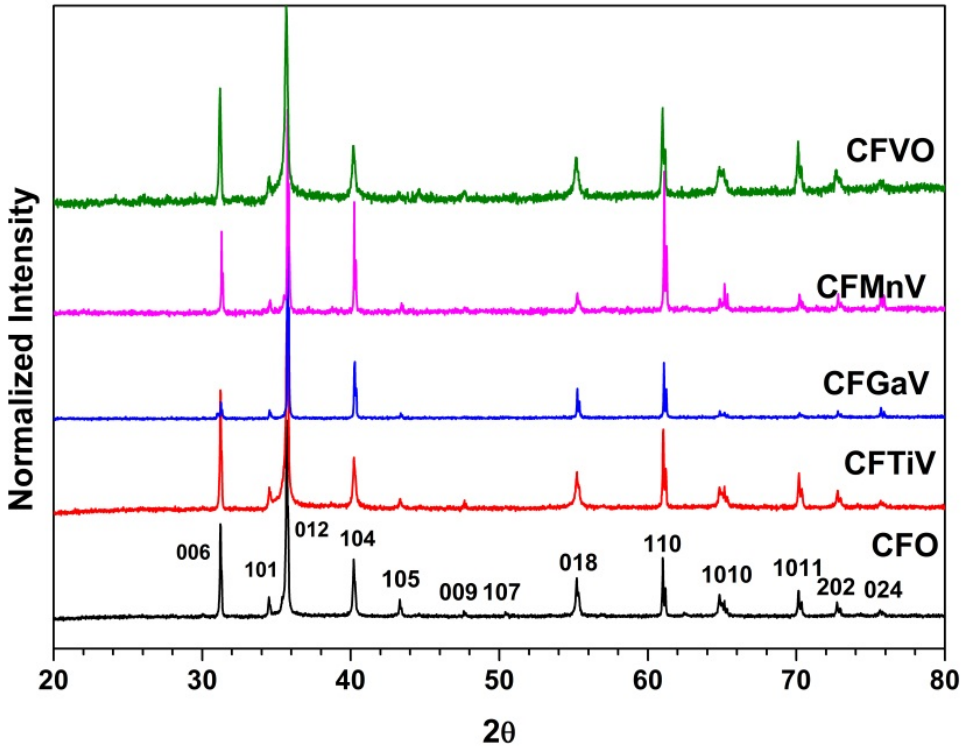

Figure 3.1: XRD-patterns of pure $CuFeO_2$ and doped samples

It is clear from the above figure that all the prepared samples revealed a single delafossite phase with confirmed rhombohedral structure (space group R-3m (no. 166)), and within the experimental limits no impurity peaks were detected. Further to confirm the experimental results Rietveld refinement method was performed to refine the structural and cell parameters by means of Fullprof software (figure 3.2) [9].

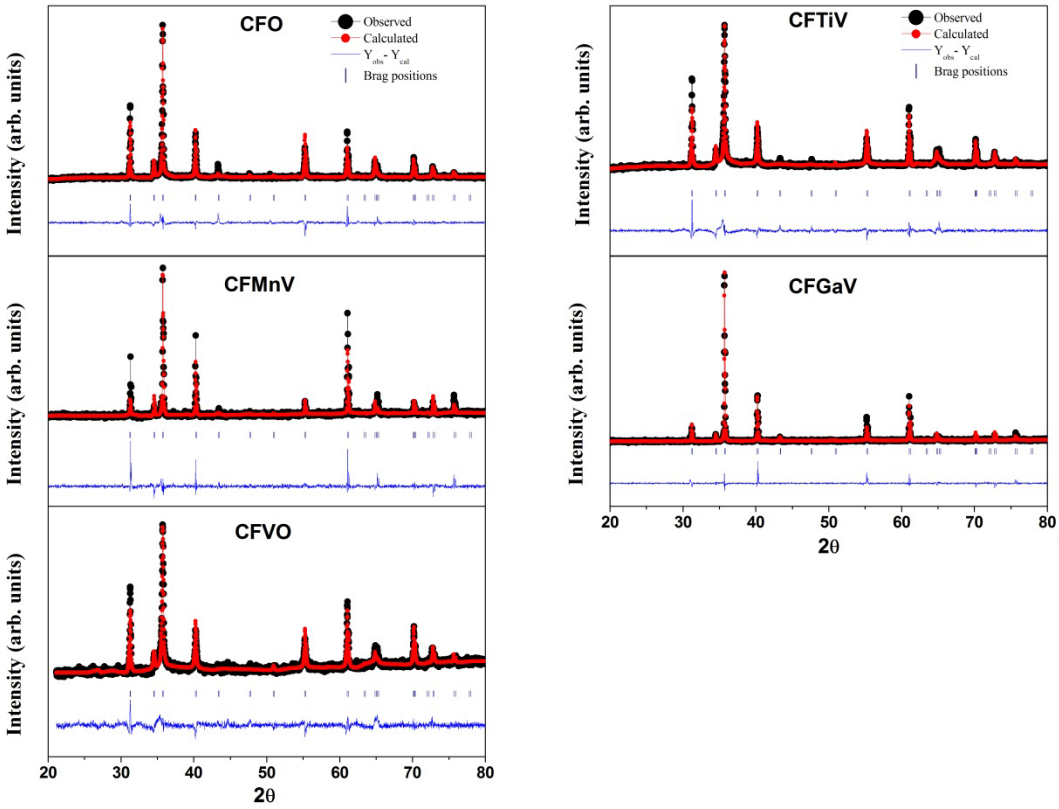

Figure 3.2: Experimental X-ray powder diffraction pattern (black line) and calculated pattern (red line) for $CuFeO_2$,$CuFe_{0.96}M_{0.03}V_{0.01}O_2$(M = Ti, Ga, and Mn) and $CuFe_{0.96}V_{0.04}O_2$. The difference is given as a bottom line. The set of Bragg ticks (blue) corresponds to the $R\bar{3}m$ space group of delafossite.

The crystallographic parameters including lattice constants, reliability factors and others are tabulated in table 3.1. From the data, it is clear that the lattice parameters show minor variations which are consistent with the ionic radii of the dopants as compared to Fe^{3+} (0.64 Å). Ti^{4+} (0.68 Å) doped sample show minor increase in the unit cell parameters, whereas the dopants with smaller ionic radii show a slight decrease in the unit cell parameters [eg. Mn^{4+} (0.60 Å), Ga^{3+} (0.62 Å), and V^{5+} (0.59 Å)]. The ionic radii and ionic charge are purely based on the notion that the dopant is likely to favor a valance state having ionic radii close to the parent element radius [10]. The density of these samples show insignificant changes due to mentioned levels of doping.

Table 3.1:Crystallographic data of pure and doped $CuFeO_2$ samples

	$CuFeO_2$	CFTiV	CFMnV	CFGaV	CFVO
Space group	$R\bar{3}m$	$R\bar{3}m$	$R\bar{3}m$	$R\bar{3}m$	$R\bar{3}m$
a (Å)	3.03356(8)	3.03405(12)	3.03126(17)	3.0332(2)	3.03269(9)
c (Å)	17.1583(6)	17.1649(9)	17.1606(16)	17.1661(16)	17.156(12)
Volume ($Å^3$)	136.719	136.842	136.556	136.779	136.650
O (z)	0.11613	0.13454	0.07478	0.08648	0.13943
Density (g/cm^3)	5.517	5.501	5.615	5.527	5.532
χ^2	1.43	1.49	2.23	2.42	2.24
S	1.19	1.22	1.49	1.54	1.71

3.1.1 Particle size and strain analysis of pure and doped $CuFeO_2$

Here three different methods are used to analyze the effect of doping on the crystallite size and the lattice strain. The plot of theWilliamson-Hall method is presented in figure 3.3, the crystallite size and strain evaluated from the same is given in table 3.2. Also "size strain plot" analysis has been performed for the better evaluation of crystallite size and strain. The plot for the same is given in figure 3.4. The details of Crystallite size and strain are given and also compared with other methods in table 3.2.

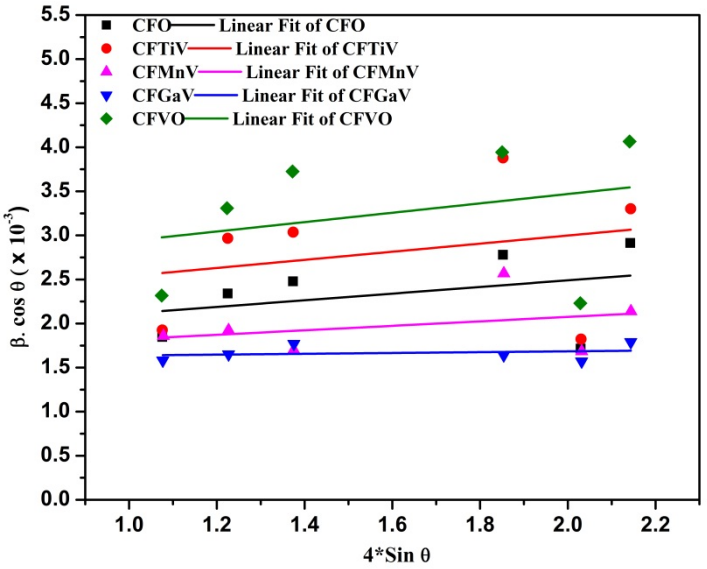

Figure 3.3: Williamson-Hall plot for $CuFeO_2$, $CuFe_{0.96}M_{0.03}V_{0.01}O_2$ (where M = Ti, Ga and Mn) and $CuFe_{0.96}V_{0.04}O_2$ samples

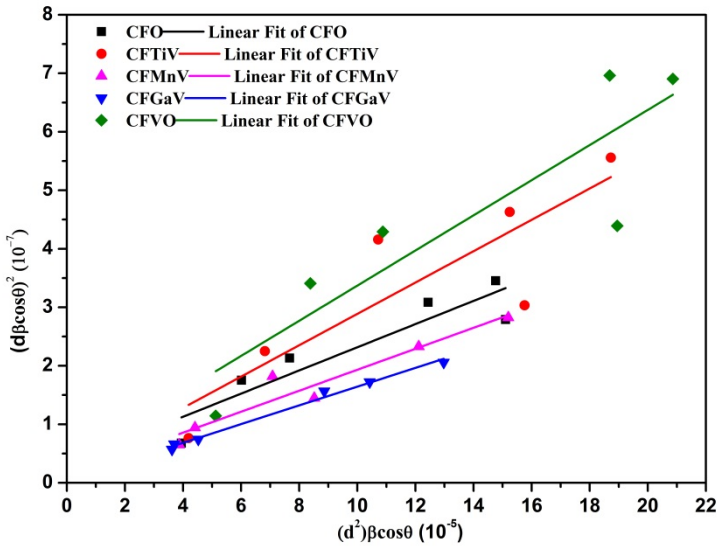

Figure 3.4: Size-strain plot for $CuFeO_2$, $CuFe_{0.96}M_{0.03}V_{0.01}O_2$ (where M = Ti, Ga and Mn) and $CuFe_{0.96}V_{0.04}O_2$

Table 3.2: Crystallite size and average strain using various methods

	Scherrer method	Williamson-Hall Method		Size-Strain plot method	
Sample	***D* (nm)**	***D* (nm)**	**ε (no unit)**	***D* (nm)**	**ε(no unit)**
CFO	61	79	3.77×10^{-4}	71	3.67×10^{-4}
CFTiV	53	66	4.60×10^{-4}	52	2.88×10^{-4}
CFMnV	72	88	2.53×10^{-4}	77	2.36×10^{-4}
CFGaV	83	87	4.52×10^{-5}	86	1.30×10^{-4}
CFVO	45	36	5.31×10^{-4}	46	3.83×10^{-4}

From table 3.2, it is clear that all the samples have a crystallite size ranging from 36 to 88 nm. In all the samples tensile type of strain is observed among which Ti and V doped samples showed the maximum strain.

3.1.2 Micro Structural Characteristics (Scanning Electron Microscopy)

The quality and morphology of well-sintered samples- of pure and doped $CuFeO_2$ are determined using scanning electron microscopy (SEM). The SEM micrographs of the sintered and annealed samples are collected at room temperature. The micrographs were collected at three different regions of the sample to ensure the correctness of the results. The collected micrographs are presented below in figure 3.5, having the same magnification of two different regions of the same sample.

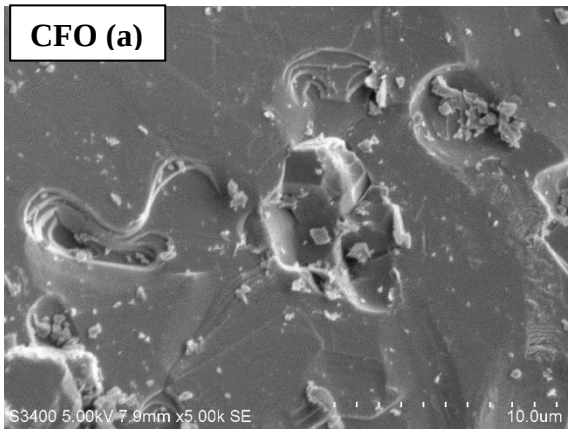
CFO (a)
S3400 5.00kV 7.9mm x5.00k SE
10.0um

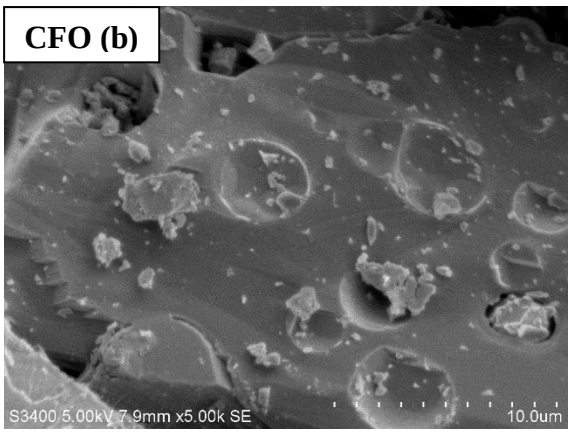
CFO (b)
S3400 5.00kV 7.9mm x5.00k SE
10.0um

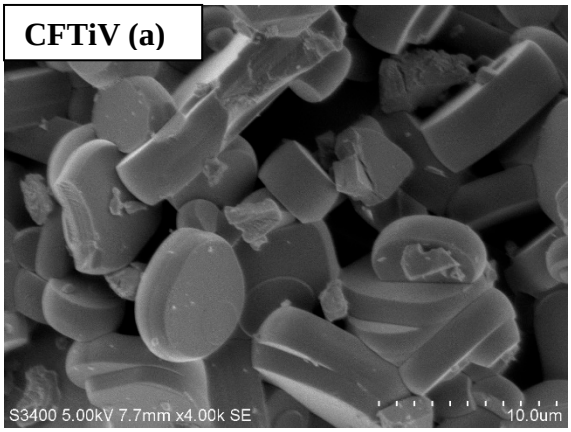
CFTiV (a)
S3400 5.00kV 7.7mm x4.00k SE
10.0um

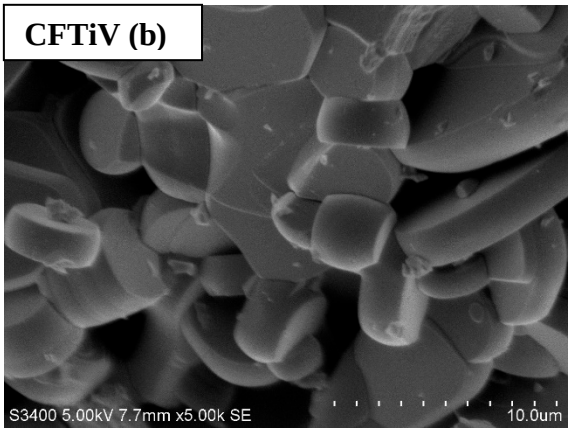
CFTiV (b)
S3400 5.00kV 7.7mm x5.00k SE
10.0um

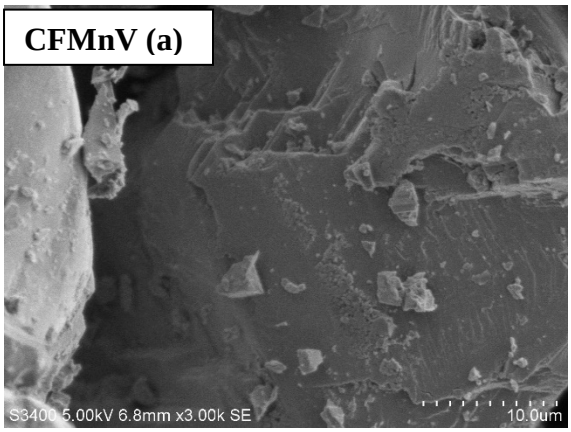
CFMnV (a)
S3400 5.00kV 6.8mm x3.00k SE
10.0um

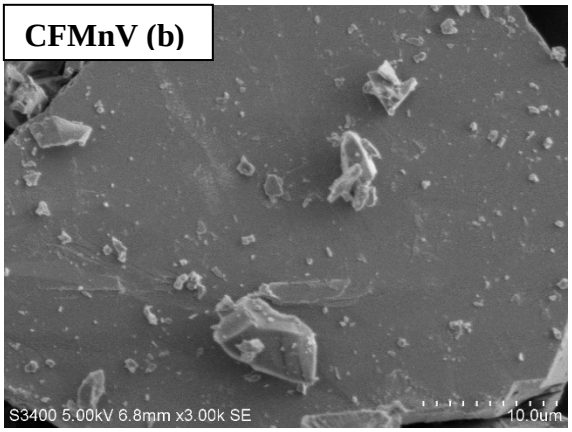
CFMnV (b)
S3400 5.00kV 6.8mm x3.00k SE
10.0um

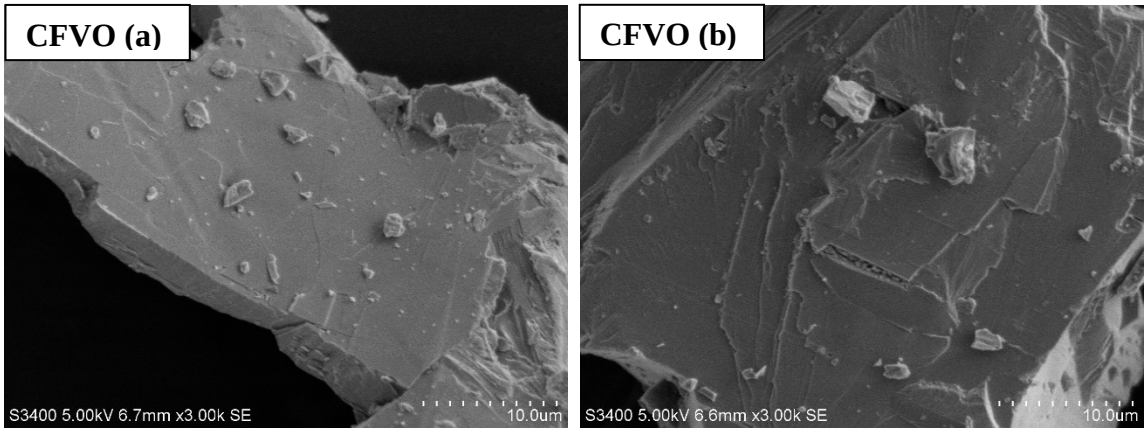

Figure 3.5: SEM micrographs of CuFeO2,$CuFe_{0.96}M_{0.03}V_{0.01}O_2$(M = Ti, and Mn) and $CuFe_{0.96}V_{0.04}O_2$.

It can be seen from the micrographs (figure 3.5) that the size of the grains is around 30 μm for CFO, CFMnV and CFVO samples. The Ti-doped sample exhibited **a** grain size of around 10 μm. Also, the crystallinity of the samples is good and well-defined grains are observed for all samples. The grain growth parameters and composition are not related systematically. These figures show flat grains with the majority of them have size around 30 μm.

In order to analyze the chemical composition of $CuFeO_2$ and one of the doped samples CFMnV, electron scanning microscope (EDS) analysis was employed. The corresponding peaks are shown in figures 3.6 (a) and (b). Further, the details of the two EDS spectra, values measured in weight and atomic percentage are listed in table 3.4.

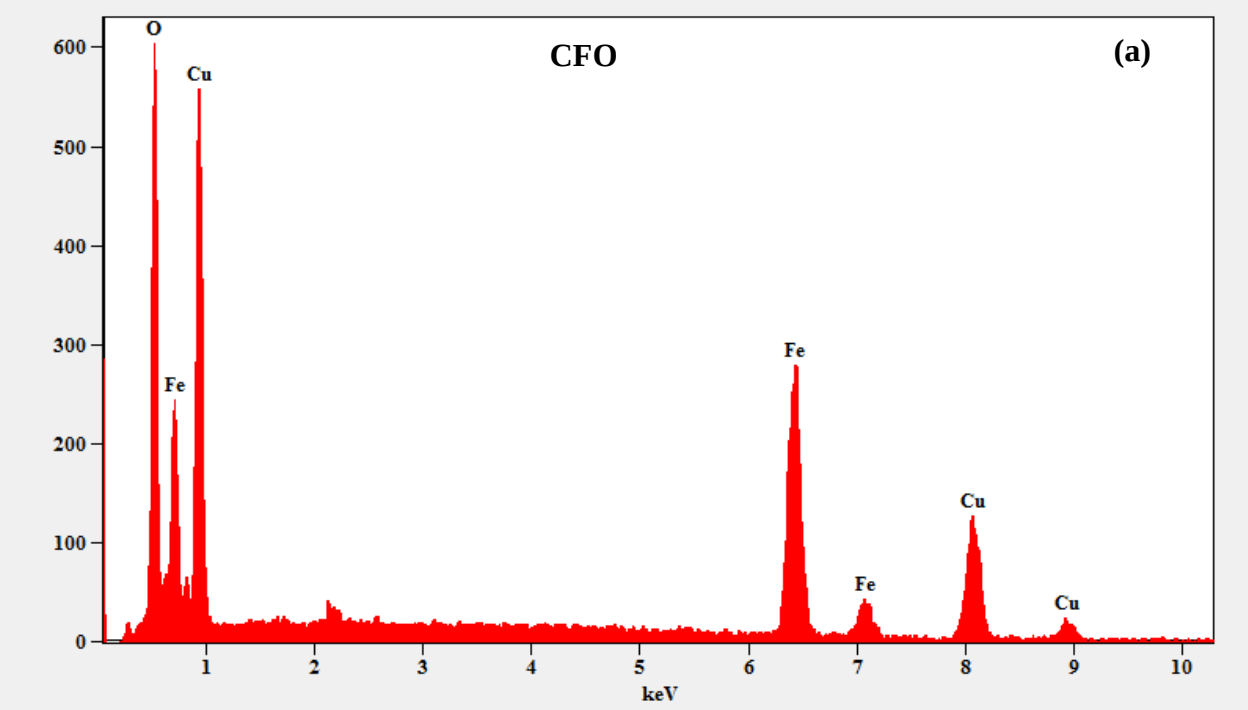

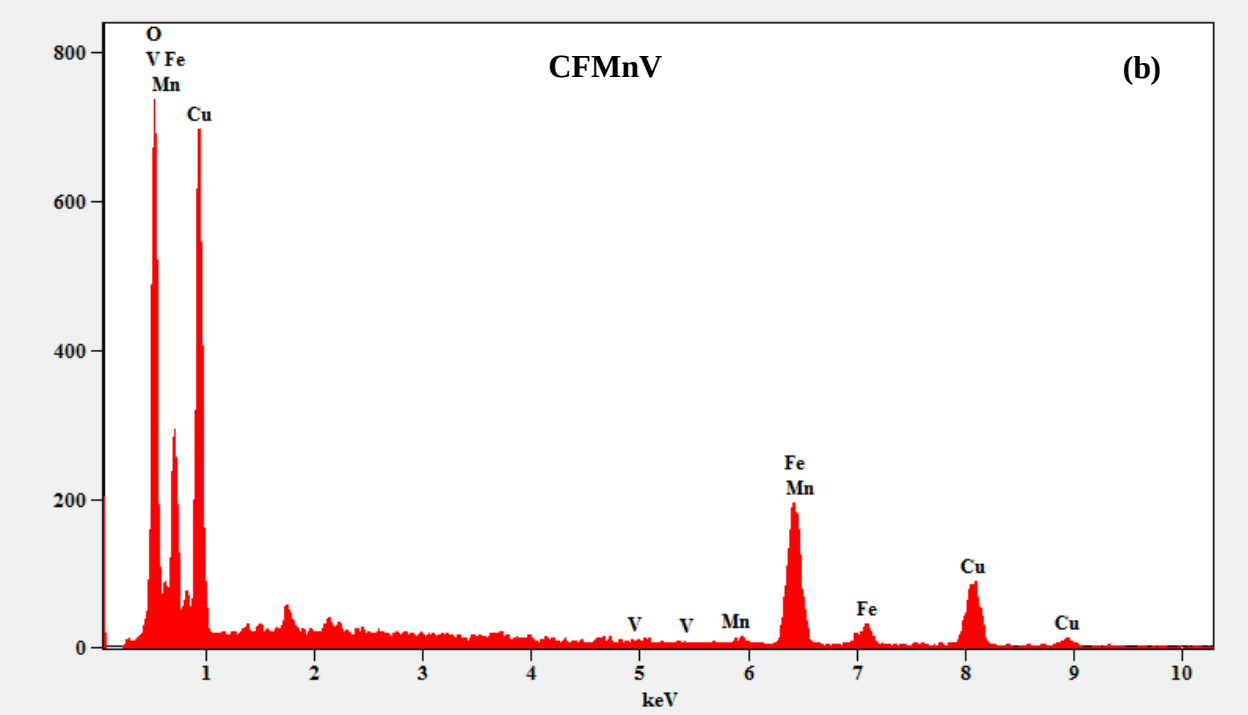

Figure 3.6: EDS spectrum for CFO (a) and CFMnV (b)

Table 3.3: Elemental analysis report of CFO and CFMnV

Element	W%	At%	Element	W%	At%
O K	22.33	51.73	***O K***	35.73	67.37
Fe K	37.00	24.55	***V K***	0.13	0.08
Cu K	40.67	23.72	***Mn K***	0.82	0.45
--	--	--	***Fe K***	31.39	16.95
--	--	--	***Cu K***	31.92	15.15
Total	100.00	100.00	***Total***	100.00	100.00

3.2 X-ray diffraction (XRD) analysis of pure and doped $CuCrO_2$

The samples in this series were prepared to study the effect of doping at the Cr site in the$CuCrO_2$ compound.The XRD patterns of pure $CuCrO_2$, doped $CuCr_{0.97-x}M_{0.03}V_xO_2$ (where M = Mg, Ti, Mn, Ni, Ga and Nb; x or= 0.00 and 0.01)(CCMV) and $CuCr_{0.96}V_{0.04}O_2$ (CCVO) along with $CuCr_{1-y}Fe_yO_2$ (y = 0.03,0.06 and 0.09) (CCFe) are shown in figure 3.7. As discussed earlier chapter some of the compositions are doped with 1% Vanadium to stabilize the phase below 1100 ^oC. Also, doping has been done a maximum of up to 4% as themajority of the ions in these compounds have the same maximum doping limit [11,12].

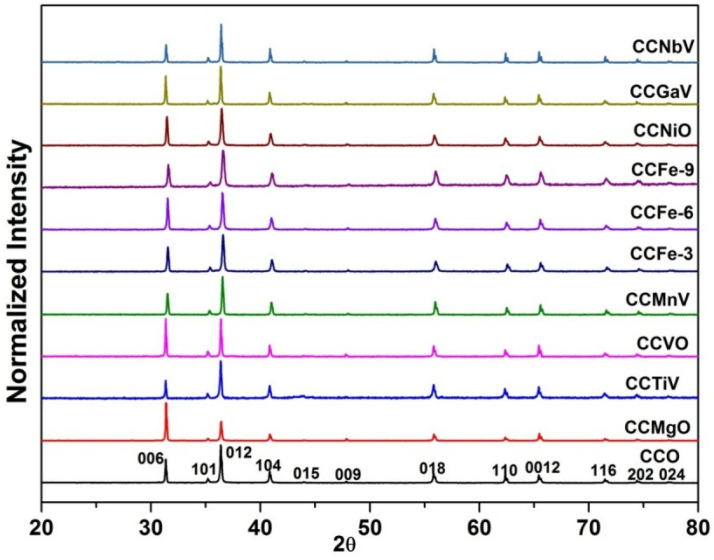

Figure 3. 7: XRD-patterns of pure $CuCrO_2$ and doped samples

As seen in the figure, no impurity peaks are seen in thediffraction pattern of the studied samples**.** The rhombohedral structure is confirmed with space group R-3m (space group no. 166) as reported earlier by others [11–17]. A line broadening and positional shift have beenobserved for the diffraction peaks (e.g. 012,104) (figure 3.8), because doping causes local strains and crystallite size variations in the parent CCO crystal structure. Further, this

can be correlated with observed changes in the strain calculation from XRD spectra and Raman spectra.

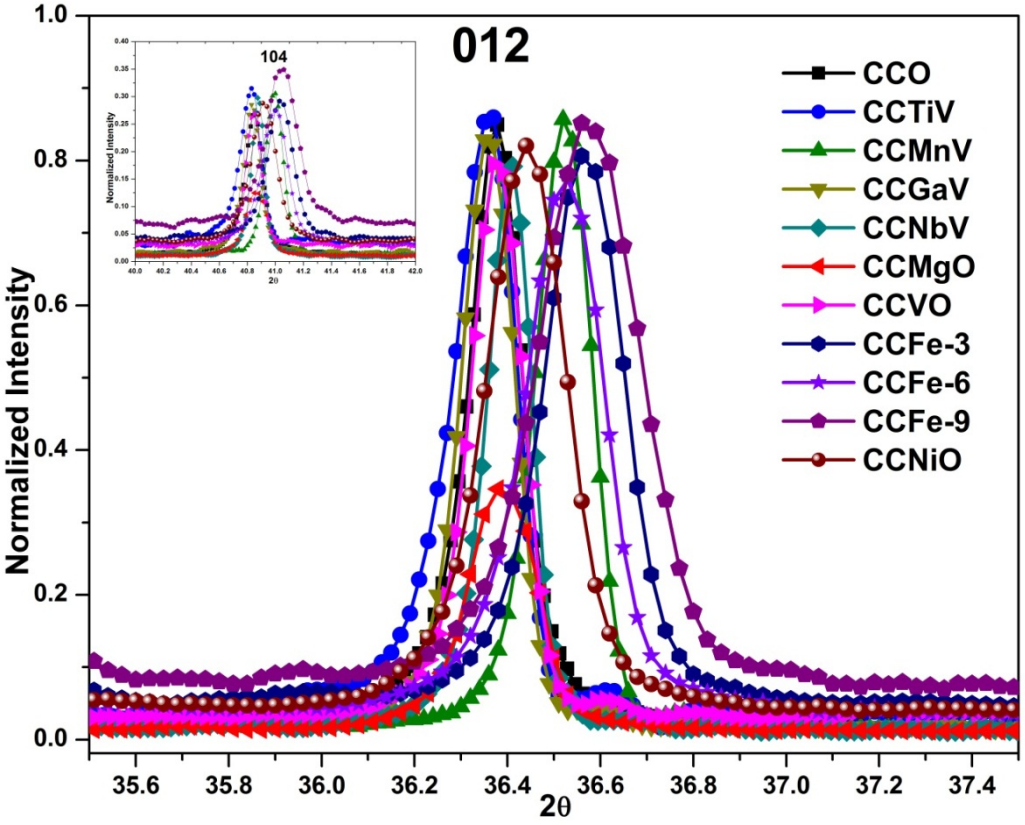

Figure 3.8: Peak 012 and 104 (inset) comparison for all the studied samples

To further ascertain the purity and to determine accurately the lattice parameters of the prepared samples the XRD patterns were further analyzed. Reitveld refinement technique was used to do anin-depth structural analysis of the samples.

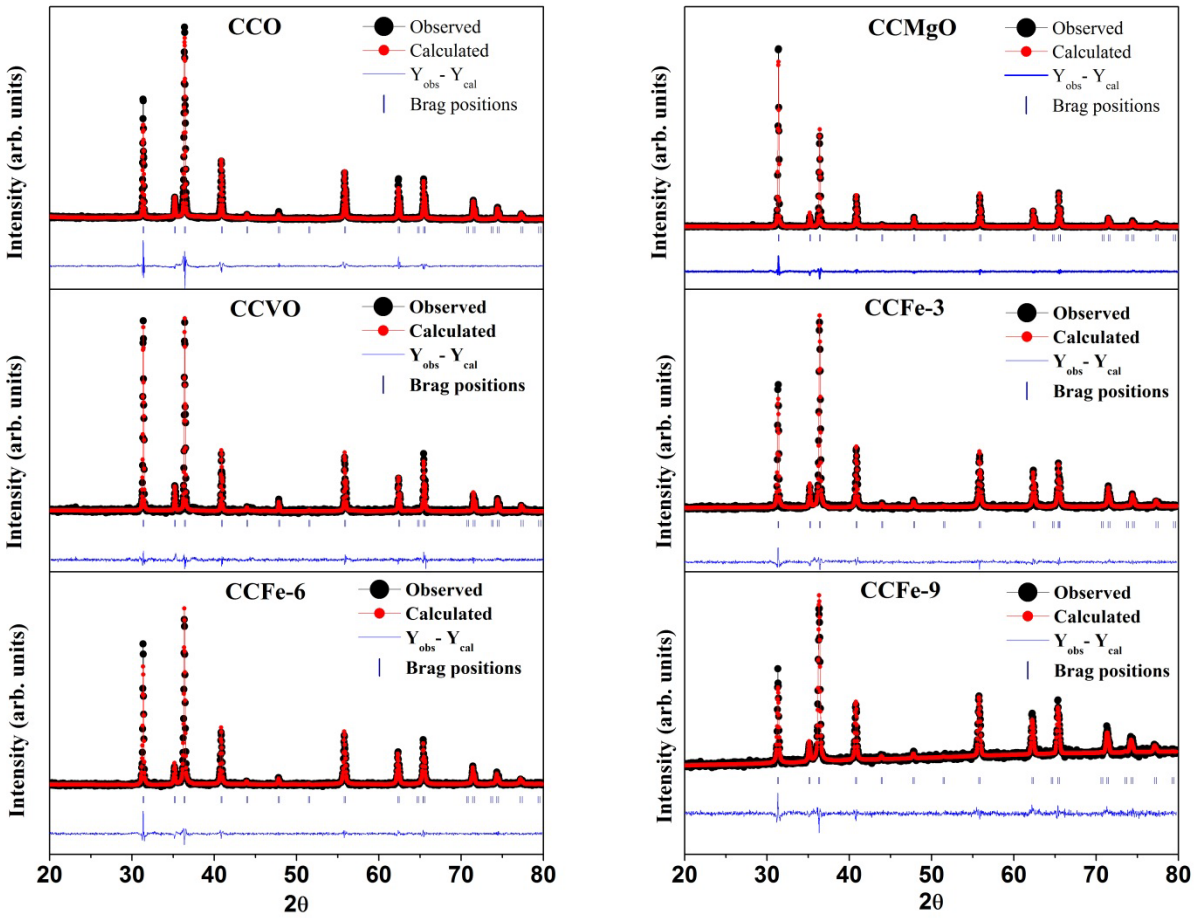

Figure 3.9: Experimental X-ray powder diffraction pattern (black line) and calculated pattern (red line) for $CuCrO_2$, $CuCr_{0.97}Mg_{0.03}O_2$, $CuCr_{0.96}V_{0.04}O_2$, and $CuCr_{1-x}Fe_xO_2$ (x = 0.03,0.06, and 0.09). The difference is given as a bottom line. The set of Bragg ticks (blue) corresponds to the $R\bar{3}m$ space group of delafossite.

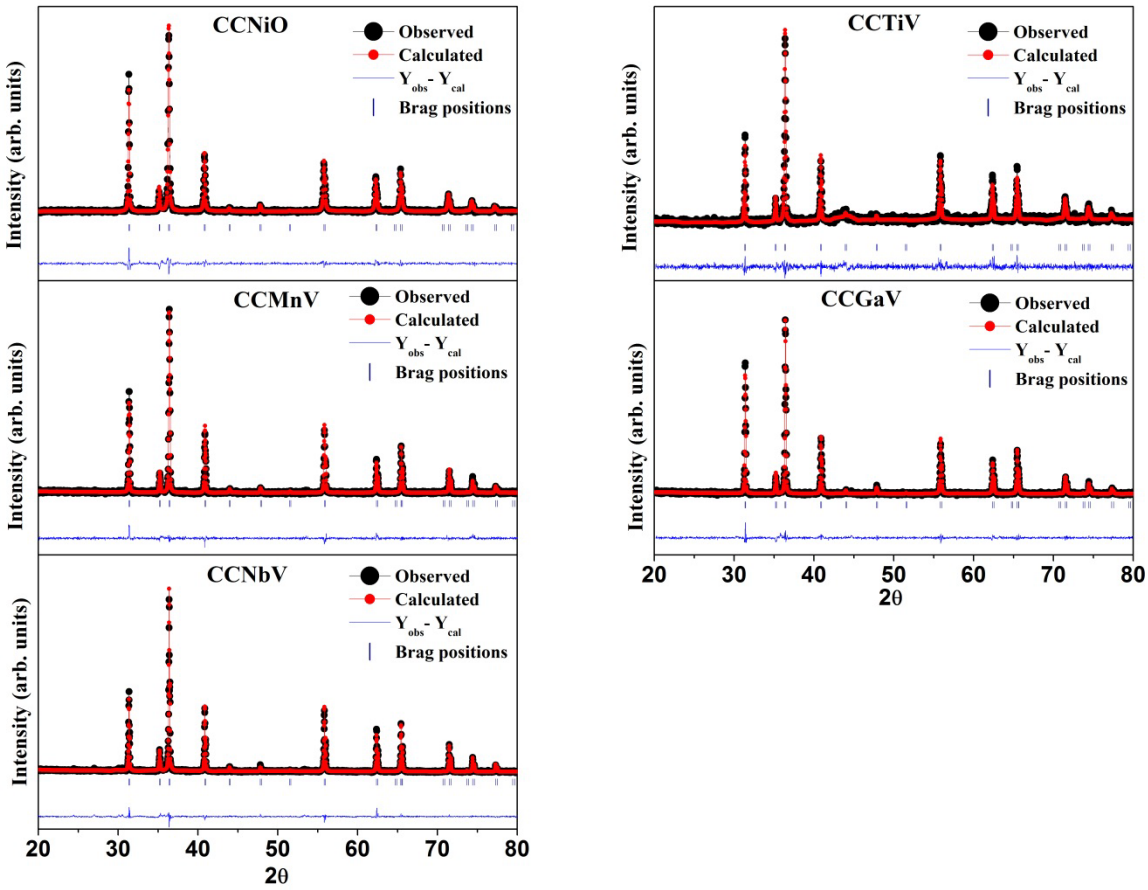

Figure 3.10: Experimental X-ray powder diffraction pattern (black line) and calculated pattern (red line) for $CuCr_{0.97}Ni_{0.03}O_2$, and $CuCr_{0.96}M_{0.03}V_{0.01}O_2$ (M = Ti, Mn, Ga, and Nb). The difference is given as a bottom line. The set of Bragg ticks (blue) corresponds to the $R\bar{3}m$ space group of delafossite.

The refined XRD patterns of the studied samples are given in figures 3.9 and 3.10 above. Refined cell and structure parameters of the obtained XRD patterns like reliability factors, lattice constants and other relevant crystallographic data are given in tables 3.4 and 3.5. Using the refined parameters bond distances and bond angles were calculated using Vesta software (ver. 3.9.9) [18]. The relevant data is tabulated in table 3.6 and 3.7.

The samples were prepared carefully under identical conditions but still, a significantly higher (006) peak was observed for the Mg and V doped samples. This could be due to the morphological differences and grains could be flat leading to preferential orientation along thec-axis during press compression. Applying the correction for preferential orientation effects on these samples showed improvement in the fitting of the data.

Table 3.4: Crystallographic data of the samples with single dopings

	$CuCrO_2$	CCMgO	CCVO	CCFe-3	CCFe-6	CCFe-9	CCNiO
Space group	$R\bar{3}m$	$R\bar{3}m$	$R\bar{3}m$	$R\bar{3}m$	$R\bar{3}m$	$R\bar{3}m$	$R\bar{3}m$
a = b (Å)	2.97437(3)	2.9755(2)	2.9744(2)	2.9752(2)	2.9779(2)	2.9817(2)	2.9791(2)
c (Å)	17.1021(2)	17.0949(7)	17.1008(10)	17.1092(12)	17.1094(11)	17.1222(14)	17.1105(11)
Volume ($Å^3$)	131.0618	131.0742	131.0197	131.157	131.397	131.828	131.5085
O (z)	0.10707	0.10986	0.10940	0.10824	0.10860	0.10733	0.10911
Cal. Density ($g\ cm^{-3}$)	5.608	5.556	5.609	5.613	5.597	5.589	5.582
R_{wp}	19.8	15.9	24.8	19.8	18.6	26.3	18.1
R_{exp}	15.5	11.9	21.3	15.9	15.3	23.0	14.7
R_B	5.26	3.45	4.32	4..87	2.39	5.75	2.55
χ^2	1.63	1.80	1.35	1.55	1.47	1.30	1.52
S	1.27	1.3	1.2	1.25	1.22	1.14	1.23

Table 3. 5: Crystallographic data of the samples with double doping

	CCTiV	CCMnV	CCGaV	CCNbV
Space group	$R\bar{3}m$	$R\bar{3}m$	$R\bar{3}m$	$R\bar{3}m$
a (Å)	2.9764(3)	2.9750(2)	2.9742(2)	2.97485(6)
c (Å)	17.1049(18)	17.0980(10)	17.0955(9)	17.1028(3)
Volume ($Å^3$)	131.226	131.0558	130.9676	131.077
O (z)	0.10738	0.1100	0.10857	0.10868
Cal. Density ($g\ cm^{-3}$)	5.595	5.611	5.631	5.653
R_{wp}	37.7	22.5	22.8	16.2
R_{exp}	34.5	20.9	19.8	12.4
R_B	7.16	4.89	4.07	4.69
χ^2	1.21	1.16	1.34	1.70
S	1.10	1.10	1.15	1.31

There were slight variations inthe unit cell parameters of doped samples compared to pure $CuCrO_2$ as shown above (Table 3.4and 3.5). Ions doped in the samples, having larger ionic radii, e.g. Ti^{4+} (0.68Å), Mg^{2+} (0.67 Å), Ni^{2+} (0.69 Å) and Fe^{3+} (0.64 Å) compared to Cr^{3+} (0.63 Å) [10], had slightly larger unit cell volume. Whereas the samples doped with the ions having slightly smaller ionic radii, e.g. Mn^{4+} (0.60Å), V^{4+}(0.63Å), Ga^{3+} (0.62 Å) and Nb^{5+}(0.63Å) [10], had a slightly smaller unit cell volume. Here the ionic charge considered is purely based on the assumption that dopant is expected to prefer a valance state whose radii is closest to the parent elements radii (Cr^{+3}, r = 0.63 Å) rather thanfurther away. Structural information such as bond angles and bond lengths are reported earlier for particular compositions [15,19], but a systematic comparison is done here for the first time along with the changes in the dopant's ionic radii and probable valance state (higher or lower) (Table 3.6 and 3.7).

Table 3.6: Selected interatomic distances and bond angles of the samples with single doping

	"Selected interatomic distances (Å)"						
	CuCrO2	**CCMgO**	**CCVO**	**CCFe-3**	**CCFe-6**	**CCFe-9**	**CCNiO**
Cu-O	1.832(4)	1.886(6)	1.871(9)	1.851(7)	1.858(6)	1.837(9)	1.867(6)
M-O	1.9969(18)	1.970(3)	1.977(5)	1.988(4)	1.986(3)	1.999(5)	1.982(3)
O-Oin	2.97473(3)	2.97550(14)	2.9744(2)	2.9752(2)	2.9779(2)	2.98170(11)	2.97909(19)
O-Oout	2.665(4)	2.582(6)	2.605(10)	2.637(8)	2.628(6)	2.664(10)	2.615(6)
(O-Oin)/(O-out)	1.1162	1.1524	1.1418	1.1282	1.1331	1.1193	1.13922
	"bond angles (degrees)"						
O-M-Oin	96.29(10)	98.11(12)	97.58(15)	96.90(14)	97.15(12)	96.44(15)	97.44(12)
O-M-Oout	83.71(10)	81.89(12)	82.42(15)	83.10(14)	82.85(17)	83.56(15)	82.56(12)
Cu-O-M	120.67(11)	119.29(13)	119.69(17)	120.21(15)	120.03(13)	120.56(16)	119.80(13)
M-O-M	96.29(14)	98.11(17)	97.60(3)	96.90(19)	97.15(17)	96.4(3)	97.44(17)

Table 3.7: Selected interatomic distances and bond angles of the samples with double doping

Selected interatomic distances (Å)				
	CCTiV	**CCMnV**	**CCGaV**	**CCNbV**
Cu-O	1.837(16)	1.881(9)	1.857(7)	1.854(6)
M-O	1.995(8)	1.972(5)	1.983(4)	1.986(3)
O-Oin	2.9764(4)	2.9750(2)	2.97424(17)	2.97485(6)
O-Oout	2.658(17)	2.589(10)	2.625(8)	2.631(6)
(O-Oin)/(O-out)	1.1197	1.1491	1.1330	1.1307
bond angles (degrees)				
O-M-Oin	96.47(18)	97.93(15)	97.14(14)	97.02(12)
O-M-Oout	83.5(18)	82.07(15)	82.86(14)	82.98(12)
Cu-O-M	120.54(19)	119.43(17)	120.03(15)	120.12(13)
M-O-M	96.5(3)	97.9(3)	97.14(19)	97.02(17)

It can be seen (Tables 3.6and 3.7) that the Cu-O bond lengths are around 1.832 Å and are in good agreement with the sum of the ionic radii (1.84 Å), assuming the two-fold coordination for Cu^{1+} (0.46 Å) and fourfold coordination for O^{2-} (1.39Å) [20]. Ti and Fe (9%) doped $CuCrO_2$ samples had higher bond lengths compared to the pristine sample, while the other samples had shorter M-O bond lengths. The changes observed in the value of lattice parameters, bond distances and/or bond angle are found to correlate more with the expected valence state-based hole or electron doping induced changes in the local electronic structure and local crystal structure rather than ionic size.

A flattened CrO_6 octahedron along the threefold axis is observed even though the entire six Cr-O bonds are equal, as the O-Cr-O bond angle departs from the ideal 90^o. To analyze this a convenient way is to use the ratio ($O\text{-}O_{in}/O\text{-}O_{out}$) defined by Doumerc et al. [21]. Here $O\text{-}O_{in}$is the distance between two oxygen's along *ab* plane, whereas $O\text{-}O_{out}$is the distance between two oxygen's of successive oxygen planes on each side of the Cr^{3+} layer. The ratio tends to increase as the Cr-O-Cr bond angles increase, which implies the compression of CrO_6 octahedra along the c-axis.

For the Fe doped samples the calculated lattice constants and volume are in good agreement with the reported values of $CuCrO_2$ (JCPDF card no.39-0247, $a = b = 2.976$ Å, $c = 17.102$ Å, $V = 131.17$ $Å^3$) and $CuFeO_2$ (JCPDF card no. 39-0246, $a = b = 3.035$ Å, $c = 17.162$ Å, $V = 136.90$ $Å^3$), and the values lies in between the two.

3.2.1 Particle size and strain analysis of pure and doped $CuCrO_2$

Results of Williamson-Hall analysis are shown infigures 3.11 and 3.12 of all the studied samples. The scattering in the data is due to the processing of the individual peaks for thedetermination of FWHM, rather than the entire spectra. Also for a better estimation of the size and strain parameters, “size-strain plot” analysis is performed and the plots are represented in figures 3.13 and 3.14. Crystallite size and the strain estimation details estimated from the Debye-Scherrer equation, Williamson-Hall analysis, and SSP method are compared in table 3.8.

It is clear fromthe data that these samples have crystallite sizesbetween 40 and 100 nm. The pristine, Mn, Ga, and Nb-doped samples negligible strain growth is observed [22,23], while the tensile type of strain is shown by the other dopants. Maximum strain values were observed for the Ti and Fe (9%) doped samples. The values obtained do vary for different methods used due to methodical differences. But the variation trends remain the same for the size and strain values.

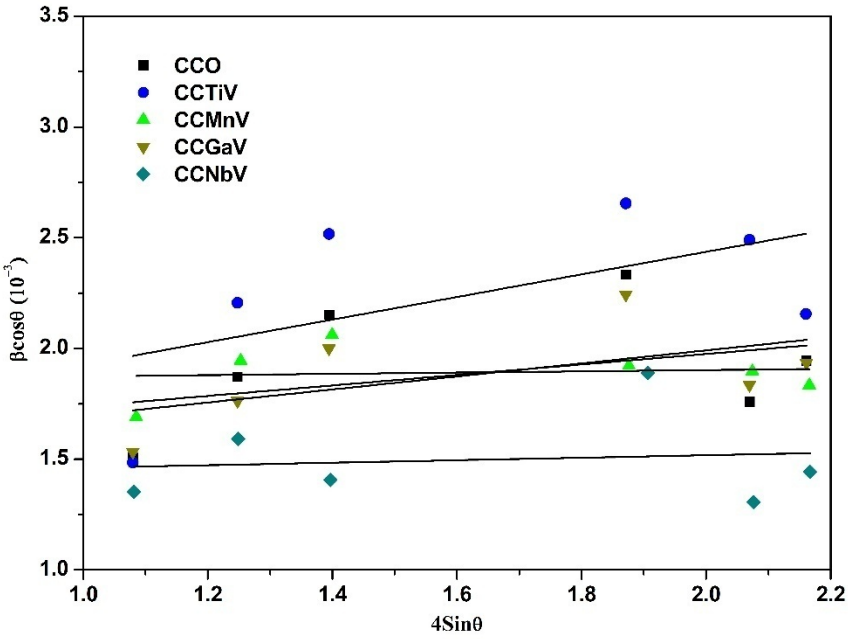

Figure 3.11: Williamson-Hall plot for $CuCrO_2$ and $CuCr_{0.96}M_{0.03}V_{0.01}O_2$ samples

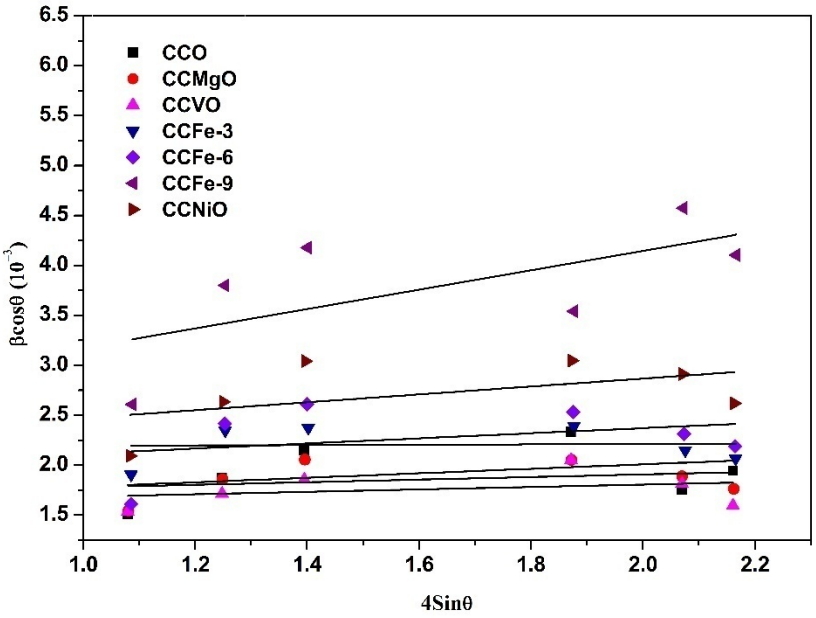

Figure 3.12: Williamson-Hall plot for $CuCrO_2$, $CuCr_{0.07}Mg_{0.03}O_2$, $CuCr_{0.07}Ni_{0.03}O_2$,$CuCr_{1-x}Fe_xO_2$ (x = 0.03, 0.06 and 0.09) and $CuCr_{0.96}V_{0.04}O_2$ samples

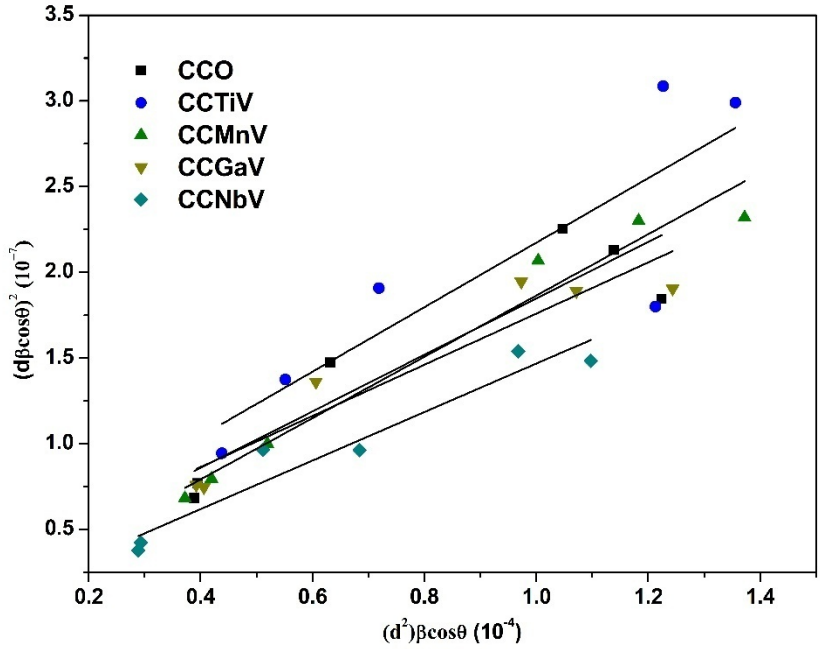

Figure 3.13: The size-strainplot for $CuCrO_2$ and $CuCr_{0.96}M_{0.03}V_{0.01}O_2$ samples

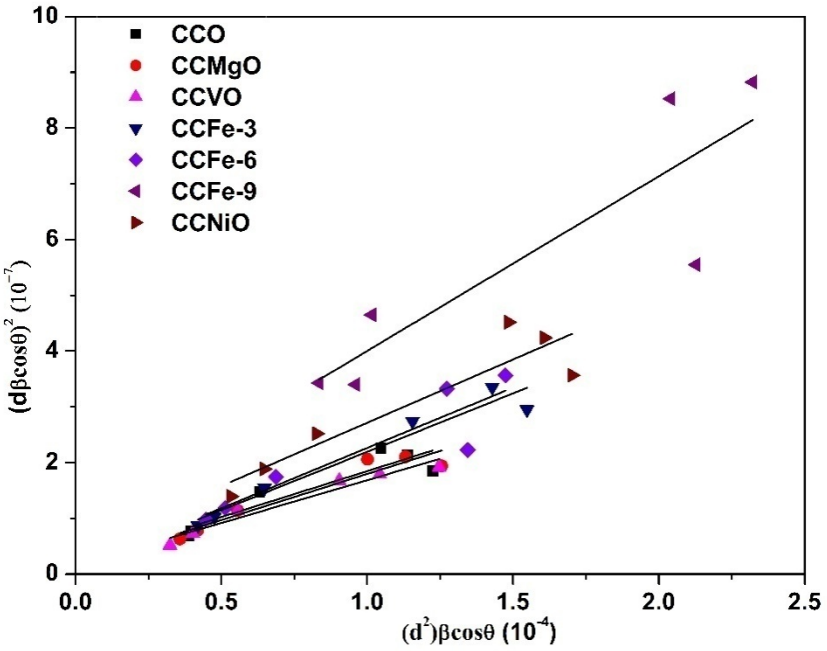

Figure 3. 14: The size-strain plot for $CuCrO_2$, $CuCr_{0.07}Mg_{0.03}O_2$, $CuCr_{0.07}Ni_{0.03}O_2$, $CuCr_{1-x}Fe_xO_2$ (x = 0.03, 0.06 and 0.09) and $CuCr_{0.96}V_{0.04}O_2$ samples

Table 3. 8: Estimated crystallite size and average strain of the studied samples with various methods

	Scherrer method	Williamson-Hall Method		Size-Strain plot method	
Sample	**D (nm)**	**D (nm)**	**ε (no unit)**	**D (nm)**	**ε(no unit)**
CCO	73	88	2.99×10^{-4}	84	2.82×10^{-4}
CCTiV	63	97	5.10×10^{-4}	74	3.41×10^{-4}
CCMnV	73	74	2.840×10^{-5}	77	1.742×10^{-4}
CCGaV	74	99	2.940×10^{-4}	93	3.26×10^{-4}
CCNbV	94	98	5.6302×10^{-5}	97	1.441×10^{-4}
CCMgO	75	84	1.29×10^{-4}	84	2.400×10^{-4}
CCVO	80	89	1.21×10^{-4}	90	2.448×10^{-4}
CCFe-3	63	63	1.83×10^{-5}	66	1.986×10^{-4}
CCFe-6	62	72	2.55×10^{-4}	65	1.816×10^{-4}
CCFe-9	33	63	9.704×10^{-4}	44	5.89×10^{-4}
CCNiO	52	67	3.95×10^{-4}	61	4.226×10^{-4}

3.2.2 Micro Structural Characteristics (Scanning Electron Microscopy)

In order to make a detailed study of effect of substitution, some of the powdered samples were investigated by SEM. For two of the samples, EDS analysis was carried out to determine the cationic content of the observed grains. The figure 3.15 shows the SEM micrographs of the samples showing the good crystallinity of the samples. Some flat grains were observed having sizes ranging from ~2-10 μm for pure, Mn and Ti-doped samples. While the larger grain size >10 μm was observed for Nb and V doped samples. The smallest grains are observed for the highest Fe (9%) substitution around ~1-5 μm.

The EDS spectrum for the samples CCCO and CCMnV with corresponding peaks are presented in the figure 3.16. The details of the two EDS spectra, values measured in weight and atomic percentage are listed in table 3.9.

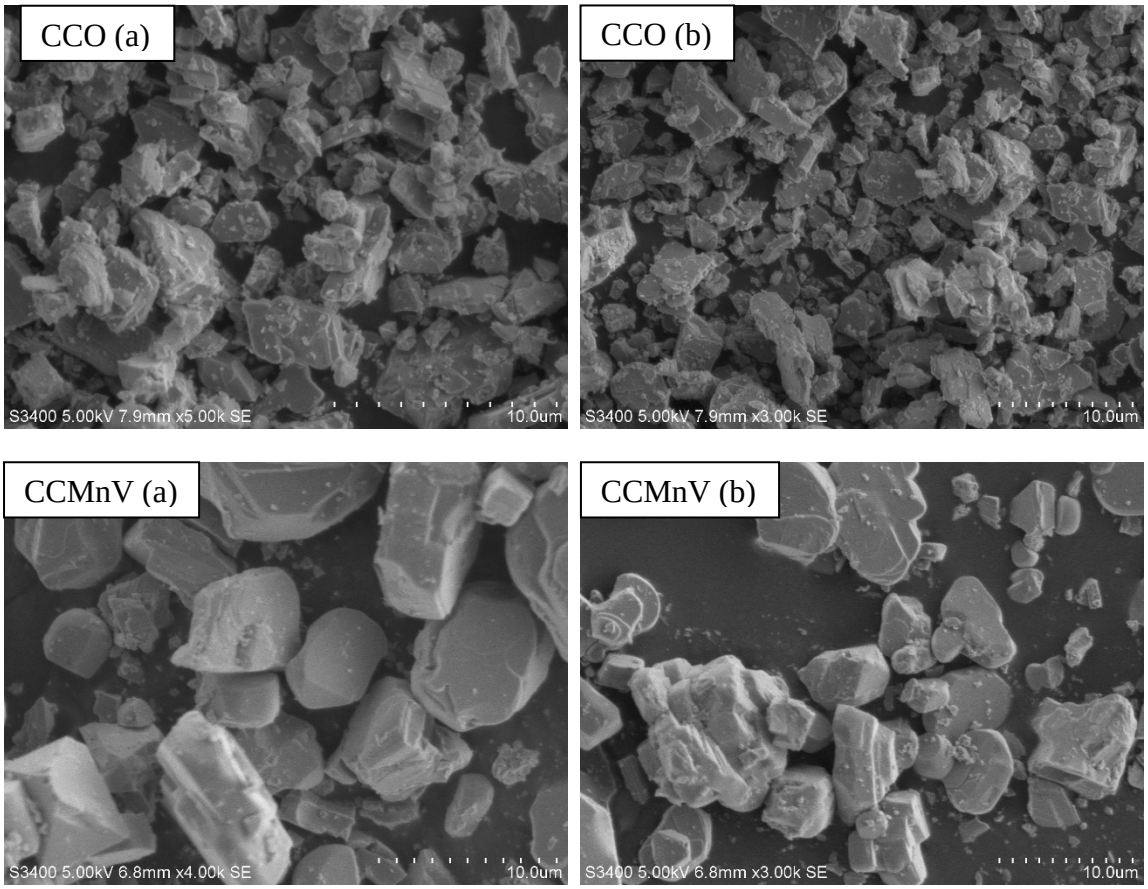

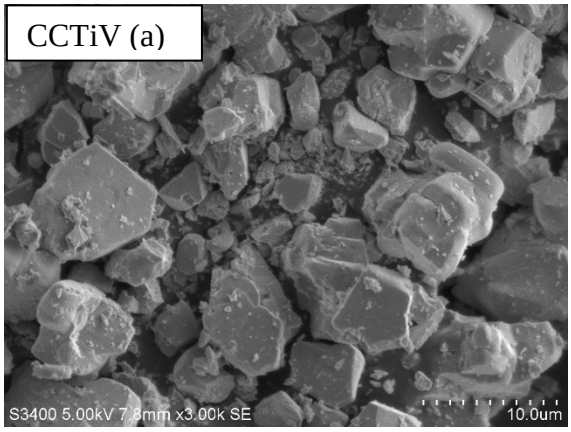
CCTiV (a)
S3400 5.00kV 7.8mm x3.00k SE
10.0um

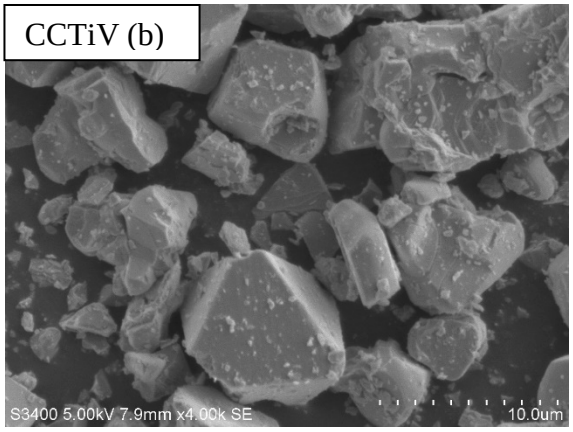
CCTiV (b)
S3400 5.00kV 7.9mm x4.00k SE
10.0um

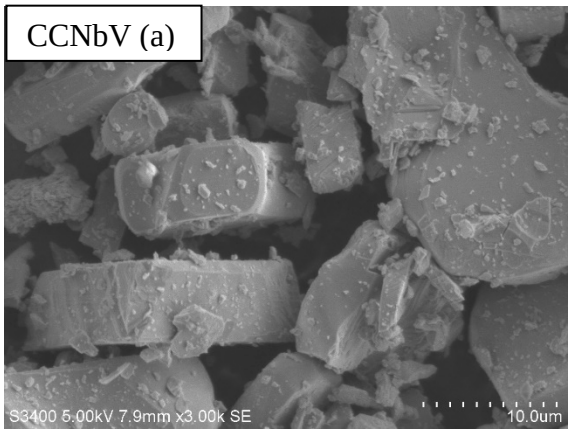
CCNbV (a)
S3400 5.00kV 7.9mm x3.00k SE
10.0um

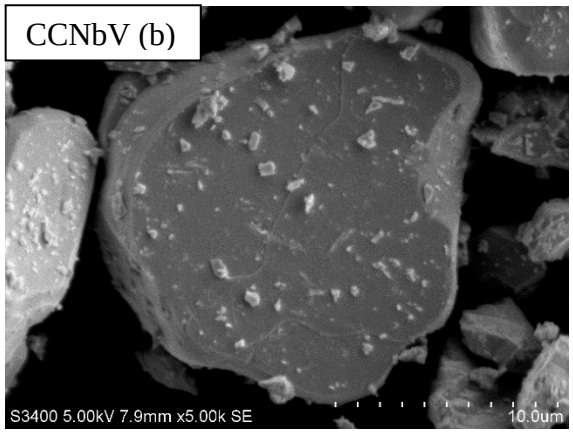
CCNbV (b)
S3400 5.00kV 7.9mm x5.00k SE
10.0um

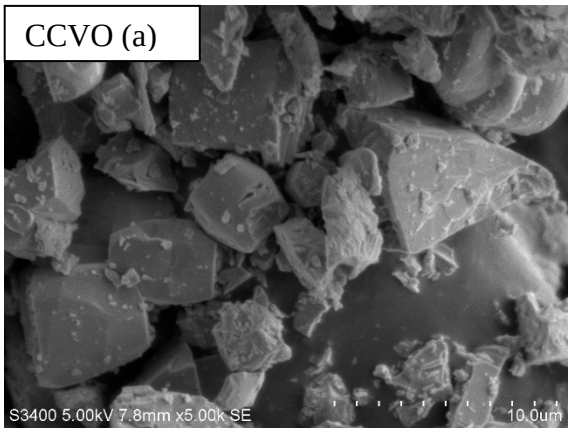
CCVO (a)
S3400 5.00kV 7.8mm x5.00k SE
10.0um

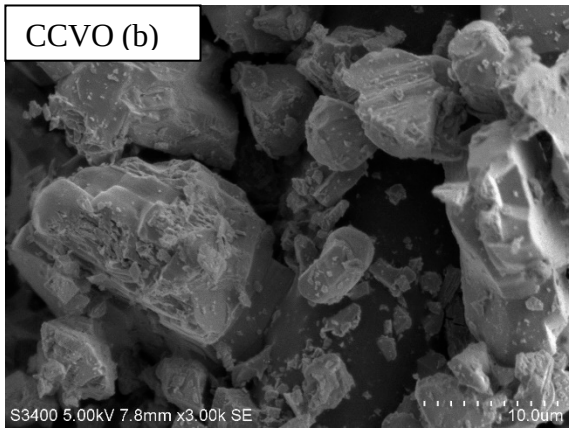
CCVO (b)
S3400 5.00kV 7.8mm x3.00k SE
10.0um

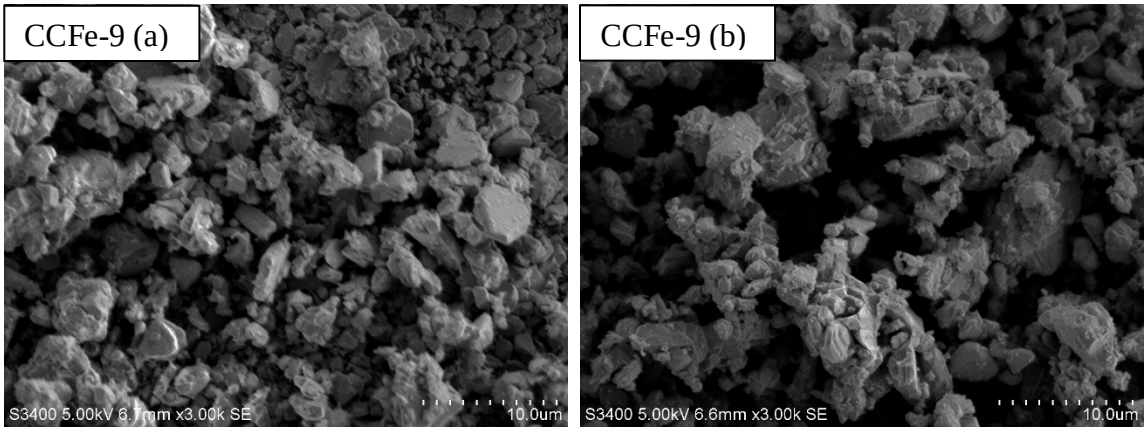

Figure 3.15: SEM micrographs of $CuCrO_2$,$CuCr_{0.96}M_{0.03}V_{0.01}O_2$(M = Mn, Ti and Nb), $CuCr_{0.96}V_{0.04}O_2$ and $CuCr_{0.91}Fe_{0.09}O_2$.

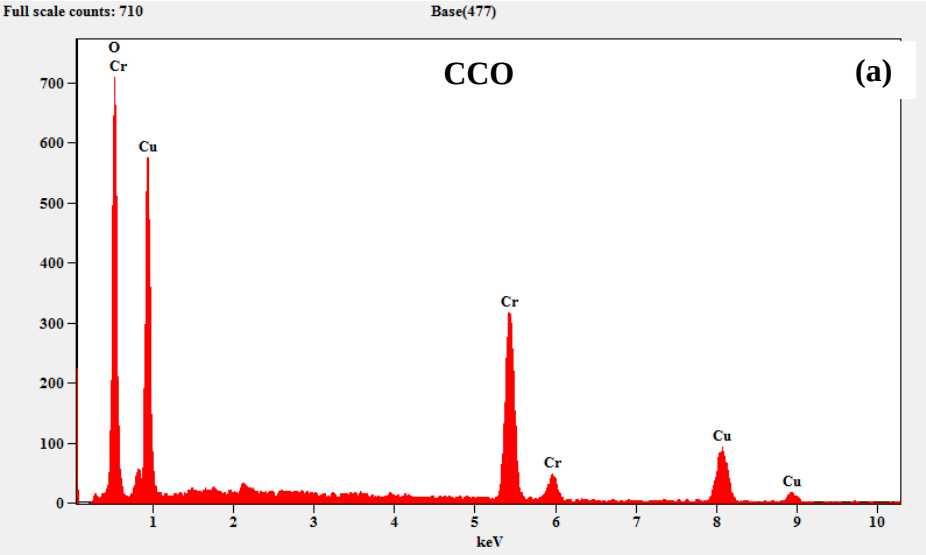

Figure 3.16: EDS spectrum for (a) CCO and (b) CCMnV

Table 3.9: Elemental analysis report of CCO and CCMnV

Element	W%	At%	Element	W%	At%
O K	33.35	64.26	***O K***	35.73	67.37
Cr K	31.71	1.79	***V K***	0.36	0.23
Cu K	34.94	16.95	***Mn K***	1.57	0.91
--			***Cr K***	29.72	18.18
			Cu K	37.10	18.57
Total	100.00	100.00	***Total***	100.00	100.00

3.3 Conclusions

Following conclusions have been dran from the studies described in this chapter:

- Pure and doped $CuFeO_2$ were prepared using the cost effective solid-state procedure involving high vacuum-sealed annealing instead of heating under inert gas. It is found that modified preparation route yields good quality samples with consistent crystallographic parameters. For pristine, Ga, and V doped samples, almost strain-free or compressive strain growth was observed. While the rest showed tensile-type strain growth. SEM micrographs confirm good crystallinity and well defined grains are observed for all samples. Also, no systematic relationship was observed between grain growth paramaeters and composition.
- Samples of pure and doped $CuCrO_2$ were successfully prepared by conventional solid-state technique exhibited single rhombohedral structure with space group R-3m. No impurity phases were detected in the Rietveld Refinement process using the Fullprof software. The obtained Cu-O bond lengths around 1.832 Å are in good agreement with the sum of ionic radii (1.84 Å), assuming twofold coordination for Cu^{1+} (0.46 Å) and fourfold coordination for O^{2-} (1.38 Å). The observed changes in the values of lattice parameters, bond distances and/or bond angle are found to correlate more with the expected valence state based hole or electron doping induced changes in the local electronic structure and local crystal structure rather than ionic size. Good crystallinity of the samples is observed in the SEM micrographs for the samples. Grain size ranging from 2-10 μm is observed for pure, Mn and Ti doped samples with rather flat grains. For Nb and V doped samples larger grain size of > 10 μm is observed, while smallest grains round 1-5 μm are observed for highest Fe (9%) substitution.

References

[1] B.D. (Bernard D. Cullity, Elements of x-ray diffraction, (1978) 555.

[2] M. Birkholz, P.F. Fewster, C. Genzel, Thin Film Analysis by X-Ray Scattering, n.d.

[3] M.A. Tagliente, M. Massaro, Strain-driven (0 0 2) preferred orientation of ZnO nanoparticles in ion-implanted silica, Nucl. Instruments Methods Phys. Res. Sect. B Beam Interact. with Mater. Atoms. 266 (2008) 1055–1061. https://doi.org/10.1016/j.nimb.2008.02.036.

[4] Q.Y. Tang, Y.M. Kan, Y.G. Li, G.J. Zhang, P.L. Wang, Effect of vanadium doping on fabrication and property of Bi4Ti3O12 ceramics, Scr. Mater. 54 (2006) 2075–2080. https://doi.org/10.1016/J.SCRIPTAMAT.2006.03.008.

[5] D.E. WITTMER, R.C. BUCHANAN, Low-Temperature Densification of Lead Zirconate-Titanate with Vanadium Pentoxide Additive, J. Am. Ceram. Soc. 64 (1981) 485–490. https://doi.org/10.1111/J.1151-2916.1981.TB09902.X.

[6] H. Dai, X. Xie, Z. Chen, F. Ye, T. Li, Y. Yang, Microstructure evolution and magnetic properties of Eu doped CuFeO2 multiferroic ceramics studied by positron annihilation, Ceram. Int. 44 (2018) 13894–13900. https://doi.org/10.1016/j.ceramint.2018.04.237.

[7] T. Nozaki, K. Hayashi, T. Kajitani, Thermoelectric Properties of Delafossite-Type Oxide $CuFe_{1-x}Ni_xO_2$ ($0 \leq x \leq 0.05$), J. Chem. Eng. JAPAN. 40 (2007) 1205–1209. https://doi.org/10.1252/JCEJ.07WE146.

[8] T. Nozaki, K. Hayashi, T. Kajitani, Mn-substitution effect on thermal conductivity of delafossite-type oxide CuFeO 2, J. Electron. Mater. 39 (2010) 1798–1802. https://doi.org/10.1007/s11664-010-1135-2.

[9] J. Rodríguez-Carvajal, Introduction to the Program FULLPROF: Refinement of Crystal and Magnetic Structures from Powder and Single Crystal Data, (n.d.).

[10] R. Weast, CRC handbook of chemistry and physics : a ready-reference book of chemical and physical data, 59th ed., 1978-1979., CRC Press, Cleveland OH, 1978.

[11] İ.C. Kaya, M.A. Sevindik, H. Akyıldız, Characteristics of Fe- and Mg-doped CuCrO2 nanocrystals prepared by hydrothermal synthesis, J. Mater. Sci. Mater. Electron. 27 (2016) 2404–2411. https://doi.org/10.1007/s10854-015-4038-4.

[12] T. Okuda, N. Jufuku, S. Hidaka, N. Terada, Magnetic, transport, and thermoelectric properties of the delafossite oxides CuCr1-xMgxO2 (0 x 0.04), Phys. Rev. B - Condens. Matter Mater. Phys. 72 (2005). https://doi.org/10.1103/PhysRevB.72.144403.

[13] S.Y. Zheng, G.S. Jiang, J.R. Su, C.F. Zhu, The structural and electrical property of CuCr1 - xNixO2 delafossite compounds, Mater. Lett. 60 (2006) 3871–3873. https://doi.org/10.1016/j.matlet.2006.03.132.

[14] M. Amami, C. V. Colin, P. Strobel, A. Ben Salah, Al-doping effect on the structural and physical properties of delafossite-type oxide CuCrO2, Phys. B Condens. Matter. 406 (2011) 2182–2185. https://doi.org/10.1016/j.physb.2011.03.027.

[15] T. Elkhouni, M. Amami, P. Strobel, A. Ben Salah, Structural, Raman spectroscopy, and magnetic ordering in new delafossite-type oxide CuCr 1-x Ti x O 2 (0≤x≤0.1), J. Supercond. Nov. Magn. 26 (2013) 2795–2802. https://doi.org/10.1007/s10948-013-2256-7.

[16] T. Elkhouni, M. Amami, P. Strobel, A. Ben Salah, Structural and Magnetic Properties of Substituted Delafossite-Type Oxides CuCr_{1 − x}Sc_xO₂, World J. Condens. Matter Phys. 03 (2013) 1–8. https://doi.org/10.4236/wjcmp.2013.31001.

[17] M. Amami, F. Jlaiel, P. Strobel, A. Ben Salah, Synthesis, structural and magnetic studies of the CuCr1-xRh xO2 delafossite solid solution with 0 ≤ x ≤ 0.2, Mater. Res. Bull. 46 (2011) 1729–1733. https://doi.org/10.1016/j.materresbull.2011.05.033.

[18] K. Momma, F. Izumi, VESTA 3 for three-dimensional visualization of crystal, volumetric and morphology data, Urn:Issn:0021-8898. 44 (2011) 1272–1276. https://doi.org/10.1107/S0021889811038970.

[19] K. El Ataoui, J.P. Doumerc, A. Ammar, J.C. Grenier, L. Fournès, A. Wattiaux, M. Pouchard, Delafossite oxides containing vanadium(III): Preparation and magnetic properties, Solid State Sci. 7 (2005) 710–717. https://doi.org/10.1016/j.solidstatesciences.2004.11.030.

[20] R.D. Shannon, Revised Effective Ionic Radii and Systematic Studies of Interatomie Distances in Halides and Chaleogenides, 1976.

[21] J.-P. Doumerc, A. Ammar, A. Wichainchai, SUR QUELQUES NOUVEAUX COMPOSES DE STRUCTURE DE TYPE DELAFOSSITE, 1987.

[22] A. Khorsand Zak, W.H. Abd. Majid, M.E. Abrishami, R. Yousefi, X-ray analysis of ZnO nanoparticles by Williamson-Hall and size-strain plot methods, Solid State Sci. 13 (2011) 251–256. https://doi.org/10.1016/j.solidstatesciences.2010.11.024.

[23] R. Sivakami, S. Dhanuskodi, R. Karvembu, Estimation of lattice strain in nanocrystalline RuO2 by Williamson-Hall and size-strain plot methods, Spectrochim. Acta - Part A Mol. Biomol. Spectrosc. 152 (2016) 43–50. https://doi.org/10.1016/j.saa.2015.07.008.